ASCE

Fracture Mechanics–Based Fragility Assessment of Pre-Northridge Welded Column Splices

Aditya Jhunjhunwala, S.M.ASCE[1]; and Amit Kanvinde, M.ASCE[2]

Abstract: A framework to assess the fracture fragility of partial joint penetration (PJP) welded column splices in steel moment frames constructed before the 1994 Northridge earthquake is presented. These pre-Northridge splices feature low flange penetration of the PJP welds, and low-toughness weld materials, such that they are considered susceptible to fracture with possible catastrophic consequences. Estimating their fracture risk is especially important, given that retrofitting them is highly disruptive to building operations. The presented framework addresses shortcomings of previous research and performance assessment guidance that does not consider key mechanistic or statistical effects. To accomplish this, three-dimensional fracture mechanics finite-element simulations are conducted to assess fracture toughness demands. These demands are then interpreted through a master curve–based approach that rigorously considers spatial randomness and weakest-link sampling of weld toughness properties, along with the uncertainty in estimation of these properties. The framework is implemented in a tool which automates the entire process, facilitating application in a professional setting. The tool (and the underlying framework) is demonstrated on a range of splice configurations to examine the effects of configuration, loading, and material parameters. Limitations are outlined. **DOI: 10.1061/JSENDH.STENG-11749.**

Author keywords: Column splices; Connections; Fracture.

Introduction

Steel moment resisting frames (SMRFs) are used widely as lateral load–resisting systems in seismic regions in the United States and elsewhere. The 1994 Northridge earthquake revealed the susceptibility of SMRF connections to fracture (SAC Joint Venture 1995a, b). Such fractures, observed mainly in welded beam-column connections, were brittle and attributed to a combination of low-toughness base and weld filler materials and stress raisers at the connections due to welding defects and discontinuities (Fisher et al. 1995; Kaufmann et al. 1997). Subsequent research (e.g., Maison et al. 1996) resulted in comprehensive revisions to design considerations (SAC Joint Venture 2000a) that mandated the use of materials with higher toughness, as well as improved connection design and weld practices to mitigate fracture. This research was predominantly focused on welded beam-column connections, although similar issues were also identified in column splice connections. Column splice connections are used in SMRFs either when the section size needs to be changed over the height of the structure or when the length of the section is not sufficient. In the pre-Northridge era (1960–1994), a large majority of column splice connections in SMRFs featured partial joint penetration (PJP) welds in the flanges and PJP welds or bolted connections in the web. Fig. 1(a) is a schematic of a typical pre-Northridge welded splice detail; Fig. 1(b) shows the typical splice locations in the frame.

Referring to Fig. 1(a), the unfused region of the PJP flange acts as a flaw under tensile loads, greatly raising stresses in the surrounding material, including the weld. Typical flange penetration in these pre-Northridge details [defined in Fig. 1(a)] is on the order of 25%–75%, implying that a large unfused region, with a width a, is usually present (Nudel et al. 2013). Base as well as weld filler materials used during this period have Charpy V-notch (CVN) impact energy of 6.8–13.6 J (5–10 ft-lb) at 21.1°C (70°F) (Fisher et al. 1995; Kaufmann et al. 1996, 1997), which is significantly lower than the CVN impact energy mandated by current standards (AISC 2016), which is 54.2 J (40 ft-lb) at 21.1°C (70°F). Fracture mechanics analysis by Nuttayasakul (2000) and Stillmaker et al. (2016) indicates that the flanges in these details (owing to the combination of large flaw sizes and low-toughness materials) are susceptible to fracture at fairly low tensile stresses of 70–140 MPa (10–20 ksi). Nonlinear response history analysis (NLRHA) by Galasso et al. (2015), Shaw et al. (2015), and Shen et al. (2010) indicates that the likelihood of exceeding these stresses is high, even at moderate levels of shaking. Referring to Fig. 1(b), the splices are usually located in the central region of the column, at some distance from floor levels, where flexural demands due to first-mode response are anticipated to be low. However, the NLRHA (Galasso et al. 2015; Shaw et al. 2015; Shen et al. 2010) reveals that a combination of single-curvature bending of the columns (due to higher mode effects) and overturning produces tensile stresses that can overcome the compressive prestress due to gravity loads and induce splice fracture. These studies estimate the risk of splice fracture to be unacceptably high [return periods for fracture ranging 75–400 years in four-story frames and 87–156 years in 20-story frames studied by Galasso et al. (2015)]. Frame simulations conducted in professional practice (Nudel et al. 2013) also reveal that flange stresses under moderate levels of shaking (corresponding to a hazard level with return period of 475 years) are significantly higher than expected fracture capacities as inferred from simplified fracture mechanics.

These observations are disquieting for three reasons: (1) splice fracture is likely to be catastrophic due to the potential loss of

[1]Graduate Research Assistant, Dept. of Civil and Environmental Engineering, Univ. of California, Davis, CA 95616.

[2]Professor, Dept. of Civil and Environmental Engineering, Univ. of California, Davis, CA 95616 (corresponding author). Email: kanvinde@ucdavis.edu

Note. This manuscript was submitted on June 11, 2022; approved on January 24, 2023; published online on March 30, 2023. Discussion period open until August 30, 2023; separate discussions must be submitted for individual papers. This paper is part of the ***Journal of Structural Engineering***, © ASCE, ISSN 0733-9445.

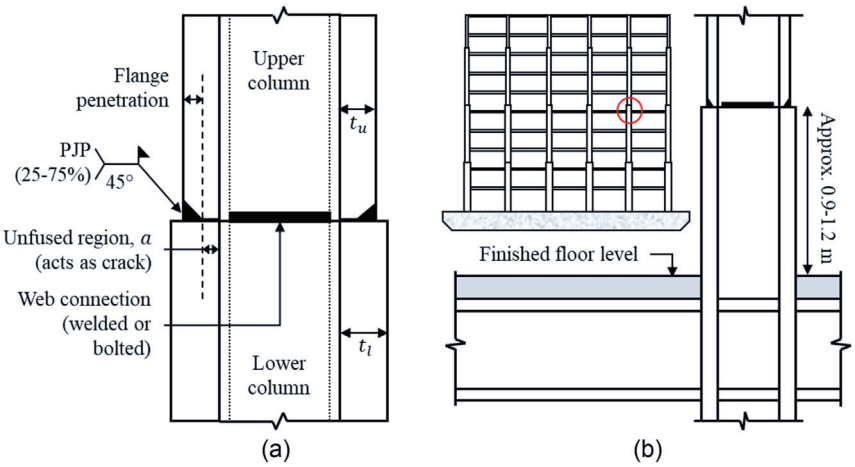

Fig. 1. (a) Typical splice detail; and (b) location of splice in frame.

gravity load–carrying capacity in the column; (2) splice connections in pre-Northridge SMRFs are largely unretrofitted; and (3) due to the location of splices in the columns, any retrofit or repair of these connections is costly and highly disruptive to building operations (Chisholm et al. 2017). Against this backdrop, it is especially critical to estimate with high confidence the fracture vulnerability of these splices because both under- and overestimation of fracture risk has serious consequences. Previous research (Stillmaker et al. 2016) and the guidelines based on it (ATC 2017) include methods for estimating the fracture capacity of pre-Northridge PJP splices, which provide reasonable first-order estimates of flange fracture stress (and have brought this problem to light) but suffer from important limitations that compromise their accuracy. Detailed in the next section, these limitations largely pertain to the use of finite-element (FE) simulations that do not consider important effects involving stress gradients and material volume sampling that are important for the assessment of brittle fracture, which is controlled by weakest-link processes. In addition, there is considerable uncertainty in the in situ fracture resistance of these welds, primarily due to the lack of standard fracture mechanics testing [e.g., K_{IC} or J_{IC} testing per ASTM (2020b)] in these deposited welds. In prior fracture mechanics studies (Nuttayasakul 2000; Stillmaker et al. 2016), the fracture toughness of the welds is indirectly inferred through a combination of correlations between CVN impact energy data (on materials used in the pre-Northridge era) and K_{IC}, correcting for loading rate and temperature effects (Barsom and Rolfe 1999). This adds further uncertainty to the predictions of fracture, so currently available approaches may not have the rigor required to assess fracture of pre-Northridge PJP-welded column splices, especially where their accuracy may inform consequential decisions regarding retrofit or risk mitigation. This need is professed by academics, professionals (Chisholm et al. 2017; Nudel et al. 2013), and the federal government [as expressed in a request for proposal for ATC (2022)]. Motivated by this, the main objectives of this paper are

- To develop a rigorous, fracture mechanics–based framework to estimate the fracture fragility of pre-Northridge PJP-welded column splices given their configuration and loading. A specific goal is to address effects not simulated by existing approaches.
- To incorporate key sources of uncertainty and volume sampling, and characterize the potential of splice fracture probabilistically.
- To demonstrate a tool that facilitates computation of the fracture fragility curve of PJP-welded splices under various types of loading.
- To apply the tool to examine response trends in pre-Northridge PJP splices; specifically, to examine sensitivity of splice fragility to various parameters (and the uncertainty in these parameters) in support of decisions regarding repair/retrofit as well as future research.

The next section outlines relevant background, focusing on current research and guidelines. This is followed by a discussion of the methodology, including finite-element fracture mechanics models, and a probabilistic simulation. The resulting fragility assessment tool is then demonstrated on various splice configurations. The paper concludes by outlining limitations of the tool.

Background and Scope

The issue of fracture vulnerability of pre-Northridge PJP-welded column splices has come to light over the last five to seven years, virtually simultaneously in academic research and professional practice. In research an important factor was a series of experimental and analytical studies (Shaw et al. 2015; Stillmaker et al. 2016) on PJP-welded column splices with toughness-rated steel and weld materials (i.e., conforming to CVN impact energy mandated by AISC 341-16 (AISC 2016)] and high-weld penetration for prospective use. These details were eventually incorporated into AISC 341-16. These studies resulted in equations to estimate the stress at which the flange would fracture given information about the configuration (i.e., thicknesses of the connected flanges and weld penetration) and the material properties (i.e., static fracture toughness K_{IC} at the given temperature). The equations were developed through regression against results from two-dimensional (2D) finite-element fracture mechanics (FEFM) simulations, which used J-integral–based fracture mechanics. The critical J-integral J_{IC} was in turn correlated with the CVN through a process outlined by Barsom and Rolfe (1999). When these equations were extrapolated (Stillmaker et al. 2016) to pre-Northridge PJP details (which had lower penetrations of 25%–75%) and lower material toughness, the estimated stresses at flange fracture were low [70–140 MPa (5–10 ksi)], especially when compared with demands estimated by NLRHA. Although these equations, along with their simplified interpretations as documented in ATC 114 (ATC 2017) and applied by Chisholm et al. (2017), have uncovered the vulnerability of pre-Northridge PJP splices, they have several limitations that impede their use in a decision support framework for retrofit. Specifically,

- The FEFM simulations (Stillmaker et al. 2016) that form the basis of the strength equations consider only 2D plane strain

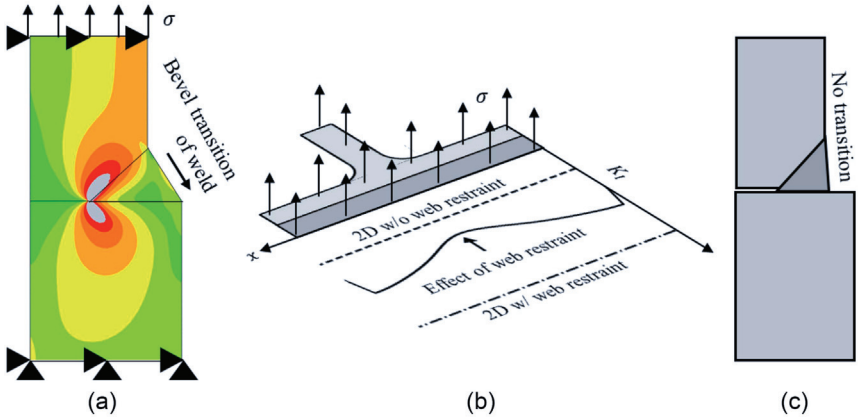

Fig. 2. Limitations of existing fracture models: (a) 2D model without web restraint showing stress contours ahead of flaw (adapted from Stillmaker et al. 2016); (b) through-width variation in fracture toughness demand K_I; and (c) no beveled transition in pre-Northridge details.

models of the splice flange [Fig. 2(a)]. These models disregard the effects of applied stress gradients both in and out of plane (due to major and/or minor axis bending), and the effect of secondary gradients in fracture toughness demands (represented by the stress intensity factor K_I) at the weld root over the width of the flange. These secondary gradients in K_I are the result of (1) edge restraint provided by the web at the center of the flange; and (2) variation in constraint from the flange tips, which are in a state of plane stress, toward the center of the flange, where the state of stress approaches plane strain. Fig. 2(b) shows the variation in fracture toughness demand through the width of the flange, as inferred from a three-dimensional (3D) simulation discussed later. As seen in the figure, these demands vary and lie between the two 2D bounds of web restraint—that is, present throughout and absent throughout.

- The FEFM simulations examine details intended for prospective post-Northridge PJP-welded splices (subsequently included in AISC 341-16). Specifically, they include a beveled transition between the thicker and thinner column flange, which is usually absent in pre-Northridge PJP splices [Fig. 2(c)]. Moreover, a large majority of these simulations also feature joint penetration ratios, in the range of 80%–90%, which are significantly greater than those used in the pre-Northridge era (25%–75%). Consequently, the equations calibrated to these FEFM data sets are not representative of the pre-Northridge details.
- It is well established (Beremin et al. 1983) that weakest-link processes often control cleavage fracture such that the likelihood of fracture is sensitive to the volume of material sampled as well as the stress gradients in this volume. In fact, the master curve approach (Wallin 1984), and associated standards in the United States (ASTM 2020a) and beyond (IAEA 2005; BSI 2019) explicitly codify this dependence. Two-dimensional fracture models and associated approaches entirely disregard this issue along with the related issue of spatial variability of material toughness in the connection, which results in a reduction in strength or deformation capacity due to weakest-link sampling.

It is important that test data on PJP-welded column splices is extremely sparse, with only one full-scale test on pre-Northridge details conducted by Bruneau and Mahin (1990) and five tests conducted more recently by Shaw et al. (2015) on prospective post-Northridge details with higher weld penetrations and notch tough materials (i.e., satisfying the requirements of AISC 341-16). As a consequence, until more experiments are conducted on PJP splices (especially pre-Northridge details), professional practice must rely on accurate computational and analytical approaches to assess the vulnerability of pre-Northridge splices. In response to this need, this study develops a framework for the fragility assessment of pre-Northridge PJP-welded column splices. The framework incorporates the state of the art in terms of fracture simulation technology and material properties, and includes potential sources of uncertainty to estimate the probability of fracture in a PJP splice connection given its configuration and loading. As implemented in a tool, the framework is developed such that its various aspects may be conveniently modified to incorporate new experimental data when available. This paper presents the scientific basis of the framework and the tool, and applies the tool to various splice configurations to derive observations beneficial to professional practice.

Fracture Mechanics–Based Fragility Assessment Methodology

Fig. 3 illustrates the overall problem statement. Referring to the figure, the problem may be decomposed into two subproblems:

- The first subproblem (in the dashed box) involves estimating the probability of fracture of a splice flange subjected to loads (i.e., axial forces, moments, and shears in both directions) applied at the ends of the column segment that includes the splice, given (1) the splice configuration, characterized in terms of upper section, lower section, flange PJP penetration, and web PJP penetration; and (2) the median fracture toughness $K_c^{(med)}$ at the lowest anticipated service temperature (LAST), which denotes the critical stress intensity factor. The problem statement assumes that the distribution of K_c may be characterized by a three-parameter Weibull distribution whose cumulative distribution function (CDF) is expressed as

$$P_f = 1 - \exp\left\{-\left(\frac{K_c - K_{\min}}{K_0 - K_{\min}}\right)^m\right\} \tag{1}$$

where $K_{\min}$ = minimum possible toughness; m = shape parameter; and K_0 (corresponding to CDF = 63.2%) = median $K_c^{(med)}$ through

$$K_0 = \frac{K_c^{(med)} - K_{\min}}{(\ln 2)^{0.25}} + K_{\min} \tag{2}$$

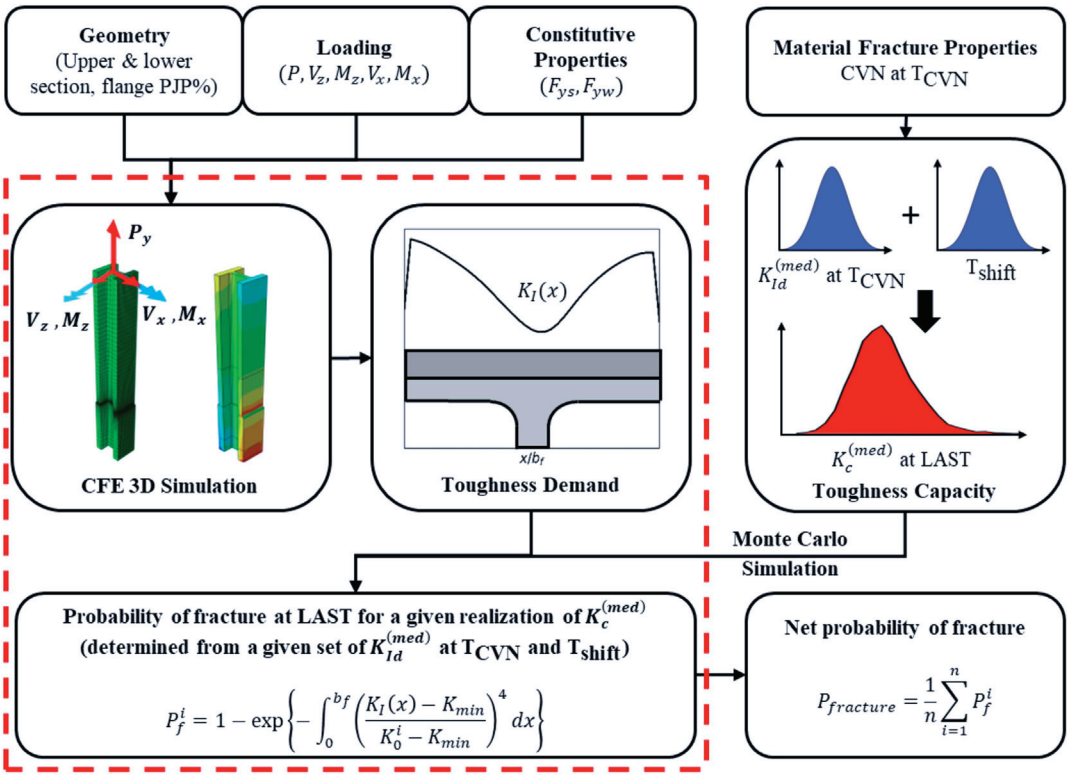

Fig. 3. Framework for fracture risk assessment.

Given these parameters, the distribution represents the spatial randomness of fracture toughness over the flange width. The Weibull distribution of fracture toughness has been extensively validated against more than a thousand experiments (e.g., Kirk 2002; Wallin 1998) and now forms the basis of ASTM E1921-20 (ASTM 2020a). In fact, the test data also strongly indicate that, for ferritic steel materials (similar to the steel considered in this study), the shape parameter may be taken as $m = 4$. Note that this spatial randomness is distinct from the *uncertainty* in the estimate of $K_c^{(med)}$ itself. This uncertainty arises because (1) direct measurements of $K_c^{(med)}$ are currently not available for pre-Northridge weld materials, implying that CVN values (which are more commonly available) must be converted to $K_c^{(med)}$ values through correlation; and (2) these CVN values are uncertain in themselves. Thus, the probability of fracture estimated in the first subproblem incorporates only the spatial randomness of K_c over the flange (conditional upon the values of $K_c^{(med)}$ and the Weibull distribution around it) and assumes deterministic geometric parameters.

- The second subproblem (outside the dashed box) involves estimation of uncertainties in the input parameter, $K_c^{(med)}$, and then integration with the first subproblem through Monte Carlo simulation. Integrating the two subproblems results in the computation of probabilities of splice fracture that include uncertainties in input material toughness as well as the effects of spatial randomness.

Once the probability of fracture is determined for a given loading, it may be generalized to a splice fracture fragility with respect to a loading parameter (e.g., the applied moment) by varying this parameter and computing the associated probabilities. Referring to Fig. 3, solving the first subproblem entails (1) FEFM simulations to estimate the fracture toughness demand (i.e., the spatial variation of toughness demand along the flaw tip in the flange) given the splice configuration and loading; and (2) computation of the probability of fracture of this splice configuration given the computed fracture toughness demands, and the spatial randomness of the fracture toughness capacity. The second subproblem entails conducting Monte Carlo simulations to incorporate the uncertainty in each input parameters to modify the computed probability of splice fracture. The next two subsections describe these subproblems and their solutions in detail.

Splice Fracture Probability Considering Spatial Randomness

Referring to the previous discussion, the first subproblem requires estimation of fracture toughness demand K_I along the crack front in the PJP splice through the width of the flange, referred to as the crack front K_I field hereafter. This is subject to some considerations. First, the applied loads, which are usually determined as the output of structural frame simulations, are considered deterministic. Second, only fracture of the flange (not the web) is considered, which is fairly realistic since the fracture toughness demands in the web are usually significantly lower. The term *splice fracture* is used interchangeably with the term *flange fracture* henceforth. Finally, the aim is to estimate the K_I field in a general way across various splice configurations (combining upper section, lower section, and flange PJP penetration) and loadings. To achieve this, 3D FEFM simulations are conducted. Fig. 4 shows one such detail [geometrically similar to that tested by Bruneau and Mahin (1990)], which is used as an example throughout this narrative.

FEFM Simulations

The FEFM simulations assume that the unfused region in the PJP splice may be represented (from the standpoint of fracture mechanics) as a sharp crack that runs along the width of the flange.

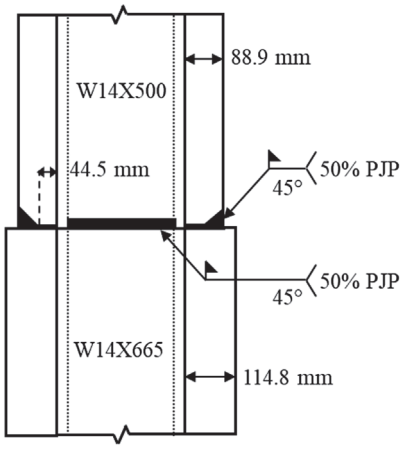

Fig. 4. Splice detail tested by Bruneau and Mahin (1990).

Consequently, the aim is to estimate fracture toughness demand along the width of the flange for a given loading and splice configuration. Note that previous simulations (Stillmaker et al. 2016) that represent the flange as a 2D plane strain problem, do not simulate this through-width variation, which arises due to a combination of biaxial bending and the effects of web restraint as well as edge effects at the free flange tips. The simulations (an example of which is shown in Fig. 5) feature the full column over the story height with the PJP splice at the splice location. The important features of the model are now briefly described:

- The simulations are conducted using the simulation platform Abaqus, which models the entire column over the story height with the splice detail subjected to column end moments and axial load. Fig. 5(a) shows the FEFM model for a splice detail representing aspects of pre-Northridge construction such as the absence of a beveled transition between the flanges.
- All elements are 20-node brick (hexahedral) elements with reduced integration (C3D20R in Abaqus). Approximately 60,000–100,000 elements are used for each model depending on section sizes.
- The faying surfaces of the splice connections are machined smooth prior to welding, so the unfused region of the flange may be assumed to be a sharp crack. Previous research (Chi et al. 2000; Kanvinde et al. 2008) suggests the validity of this assumption. Consequently, the unfused region between flanges is modeled by a 0.0254-mm (0.001-in.) width gap with a semicircular crack tip of the same diameter. The blunted crack tip, which is modeled as roughly 1/10th the expected crack tip opening displacement following McMeeking and Parks (1979), regularizes the stress field at the crack tip without affecting the accuracy of the J-integral measure.
- The crack tip mesh is refined such that the computed J-integral values do not show significant variation on further refinement; that is, mesh convergence is achieved. Table 1 shows the values of J-integral converted to the equivalent stress intensity factors using Eq. (3) for different mesh sizes in the radial direction near the crack tip. The values are for the representative detail shown in Fig. 4, subjected to (1) uniform tension; and (2) pure major axis (uniaxial) bending. Since J-integral is a far-field measure, its sensitivity to mesh size is minor. A comparably coarse mesh with a maximum element length of 0.4 mm (0.016 in.) in the radial direction is sufficient. Fig. 5(c) shows the crack tip mesh adopted for all section sizes. The element size remote from the crack tip is kept sufficiently large (on the order of half the flange thickness) to reduce the computational cost.
- The unfused parts of the web and the flanges are assigned hard contact behavior under compressive stresses.
- Both base and weld materials are simulated as elastic-plastic materials with von Mises plasticity and nonlinear isotropic hardening. The steel material A572 Grade 50 (345 MPa) was commonly specified for columns during the 1980s (SAC Joint Venture 2000b)

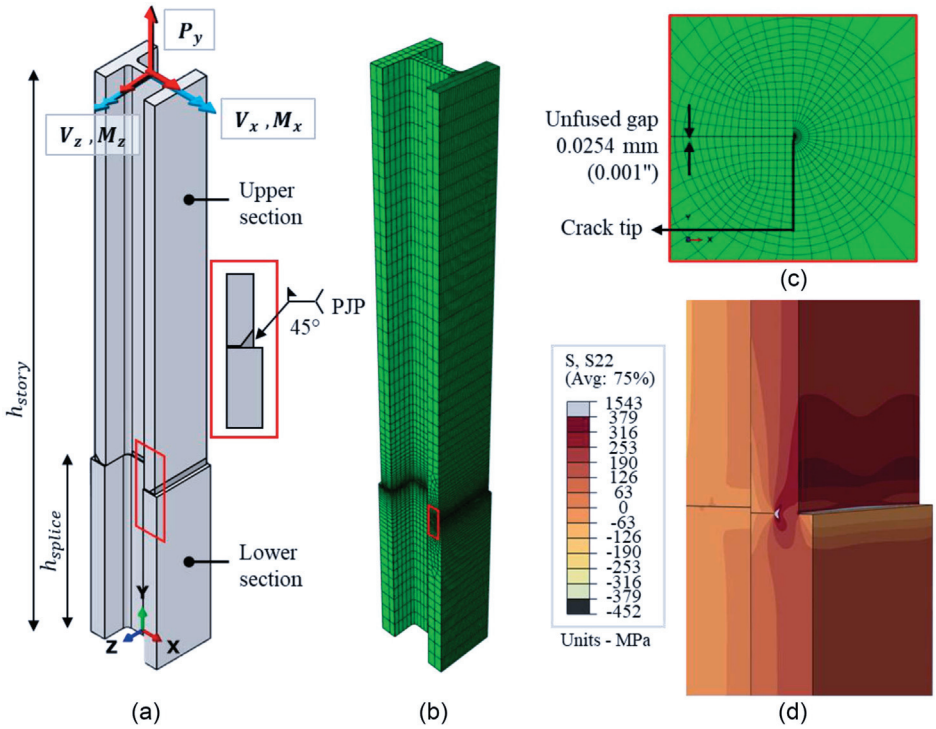

Fig. 5. FEFM simulation: (a) overall model geometry; (b) FE mesh; (c) crack tip mesh; and (d) longitudinal stress pattern near splice.

Table 1. Variation in far-field J-integral (converted to equivalent stress intensity factor, K_J) with mesh size. Maximum flange stress in upper section: 35 ksi for uniform tension and 45 ksi for pure bending

	K_J MPa$\sqrt{\text{m}}$ (ksi$\sqrt{\text{in.}}$).			
	Maximum along flange		At center	
Mesh size (mm/in.)	Uniform tension	Pure bending	Uniform tension	Pure bending
1.3 (0.051)	152.673 (138.940)	128.612 (117.043)	132.319 (120.417)	107.594 (97.916)
0.6 (0.024)	152.693 (138.958)	128.717 (117.139)	132.324 (120.421)	107.600 (97.921)
0.4 (0.016)	152.726 (138.988)	12751 (117.170)	132.334 (120.430)	107.605 (97.926)
0.2 (0.008)	152.781 (139.038)	128.800 (117.214)	132.361 (120.455)	107.631 (97.949)

and is used as the representative material for column steel in the simulations. An expected yield strength of 380 MPa (55 ksi)—determined from tension coupons extracted from the flanges of the W-shapes during the SAC investigation (Jaquess and Frank 1999)—is assigned to the steel material. The weld electrodes used in the pre-Northridge era were E70T-4 and E70T-7 flux cored arc weld with a specified ultimate tensile strength of 480 MPa (70 ksi) and were not required to meet minimum toughness requirements. The weld materials exhibited wide variability in yield strength due to variations in welding procedures. An expected yield strength of 450 MPa (65 ksi), as suggested by available data (Chi and Deierlein 2000), is assigned to the weld material. Details of the nonlinear hardening properties are provided in Stillmaker et al. (2016).

- The bottom of the column [at the lower story level shown in Fig. 5(a)], is assigned fixed boundary conditions (total fixity in the three directions), while the top of the column is free. This removes rigid body modes so that the end forces (e.g., as inferred from frame analysis) can be converted to moments, shears, and axial force at the top of the column. The loading is applied at the top surface of the column as surface pressure for axial load and moment and as traction for shear.
- For any loading condition [i.e., an applied set of P, V_z, M_z, V_x, M_x as shown in Fig. 5(a)], the loads are increased proportionally, and J-integral values are computed as the loads increase from zero up to the applied load. The domain integral capability of Abaqus is used for J-integral evaluation. The penultimate contour to any exterior surface of the model is used to minimize the contour dependence of J-integral (Brocks and Scheider 2003). The J-integral value is calculated at all the nodes along the width of the flange. The values obtained from the simulations are converted to the elastic-plastic plane strain–equivalent stress intensity factor K_J (Anderson 2017) using the following equation:

$$K_J = \sqrt{J \times E/(1-v^2)} \tag{3}$$

Eq. (3) is consistent with the computed K_J in the master curve–based framework for fracture prediction (ASTM 2020a), in which the master curve itself is calibrated from plane strain fracture toughness. The term K_I is used instead of K_J in this study to allow for a more general toughness demand—elastic or elastic-plastic.

Fig. 6 shows the K_I fields along the crack tip, through the flange width, for the representative detail (Fig. 4) when subjected to three types of loading: (1) uniform tension, (2) pure major axis (uniaxial) bending, and (3) pure biaxial bending (which introduces a stress gradient over the flange width), with no shear in each case. The bending moments and axial force for tension are selected such that

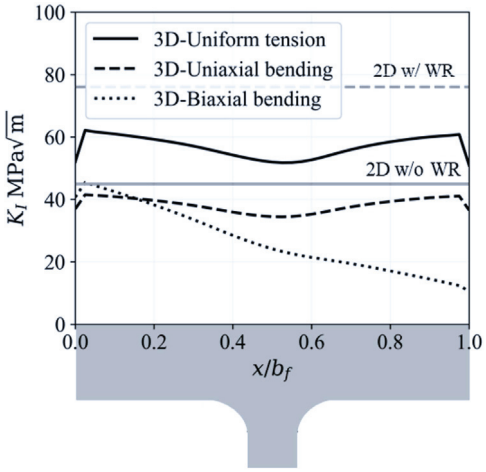

Fig. 6. Through-width variation in fracture toughness demand (WR = web restraint).

for all three loadings the maximum flange tensile stresses $\sigma_{\text{flange}}^{\max}$ (remote from the crack) are equal [117 MPa (17 ksi)]. Aside from providing a general sense of the toughness demands in the flange, Fig. 6 indicates the following:

- Biaxial bending introduces a strong gradient in the K_I field over the flange width, which is not surprising given a similarly strong gradient in the remote stress itself.
- Despite the maximum remote tensile stress in the flange being similar between the three loadings, peak K_I is different. Specifically, peak K_I due to uniform loading is roughly 37% larger than peak K_I due to biaxial bending, which in turn is 9% larger than peak K_I due to uniaxial bending. This indicates that using only the peak stress (e.g., from a frame simulation) and disregarding gradients (either in plane or out of plane) for estimating fracture toughness demand is not appropriate, even for estimation of peak K_I.
- The bounds correspond to the plane strain 2D simulations, with web restraint (2D with WR) and no web restraint (2D without WR) conditions, respectively. The uniform tension condition lies between the two, which is as expected, because the 2D simulations feature only uniform tension in the flange. However, the other two loadings are not bounded by these estimates, further emphasizing the importance of 3D effects.

It is relevant that the validity of J-integral as a fracture toughness measure was independently established through comparisons of the crack tip stress field with the well-known HRR singularity (Hutchinson 1968; Rice and Rosengren 1968), which showed that the region of crack tip yielding is significantly smaller than the J-dominance zone.

Fracture Probability Computation Using the Master Curve

The master curve (Wallin 1998) provides a rational framework for characterization of lower-shelf and lower-transition fracture toughness capacity of ferritic steels. It has two main features: (1) a statistical variation in fracture toughness capacity at a given temperature, and (2) a unique relationship between temperature and median fracture toughness. ASTM E1921-20 includes the procedure for characterizing the master curve of ferritic steels that experience the onset of cleavage cracking at elastic or elastic-plastic instabilities or both. The basic expression for the macroscopic fracture probability of a 25.4-mm (1-in.) -thick cracked specimen ("1T" per ASTM 2020a), based on a three-parameter Weibull distribution, also shown in Eq. (1), is given by (Wallin 1984)

$$P_f = 1 - \exp\left\{-\left(\frac{K_c - K_{\min}}{K_0 - K_{\min}}\right)^m\right\} \tag{4}$$

where K_c = critical fracture toughness based on elastic or elastic-plastic instability; $K_{\min}$ = lower limiting K_c below which cleavage fracture is not possible; K_0 = fracture toughness with 63.2% fracture probability of exceedance; and m = shape (or "slope") parameter. The value of $K_{\min}$ is calibrated as 20 MPa$\sqrt{\text{m}}$ (18.2 ksi $\sqrt{\text{in}\cdot}$) for ferritic steels, and the shape parameter m is taken as 4 (Wallin 1984). The temperature dependence of the median toughness capacity $K_c^{(med)}$ (corresponding to $P_f = 50\%$) is given by (Wallin 1993) as

$$K_c^{(med)} = 30 + 70e^{0.019(T-T_o)}\text{MPa}\sqrt{m} \tag{5}$$

where T_o = reference temperature. The reference temperature represents the temperature at which $K_c^{(med)}$ is equal to 100 MPa$\sqrt{\text{m}}$ (91 ksi $\sqrt{\text{in}}$. Eq. (5) is an empirical fit to transition fracture toughness data for 10 heats of nuclear reactor pressure vessel steels and weldments (Wallin 1993) and has been validated by numerous researchers for various ferritic steels (Kirk 2002 provides a summary). The value of T_o may be obtained by either solving the equation using the known $K_c^{(med)}$ value at a temperature T or from multiple K_c values at different temperatures [ASTM E1921-20 describes the full procedure). As discussed previously, the validity of the master curve has been the subject of numerous studies and is now considered canonical in fracture mechanics (ASTM 2020a; IAEA 2005) and is codified in ASTM E1921-20. Fig. 7 shows the master curve, illustrating the parameters that define the temperature dependence of median toughness capacity given by Eq. (5) as well as the fracture probability distribution function implied by Eq. (4) (which is functionally a cumulative distribution function at a given temperature). By convention, the master curve together with the associated probability distribution of fracture corresponds to a standard 1T specimen that is 25.4 mm (1 in.) thick. Generalizing this to different thicknesses or crack fronts along which K_I is variable (such as along the flange width as shown in Fig. 6) requires explicit consideration of volume-sampling effects. Following the weakest-link approach (Beremin et al. 1983; Wallin 1985), the probability of fracture for a specimen with thickness B (mm) subjected to uniform toughness demand K_I over this width may be expressed as

$$P_f = 1 - \exp\left\{-\left(\frac{K_I - K_{\min}}{K_0 - K_{\min}}\right)^4 \left(\frac{B}{25.4\text{ mm}}\right)\right\} \tag{6}$$

When toughness demand is not constant along the crack tip, Eq. (6) may be generalized to

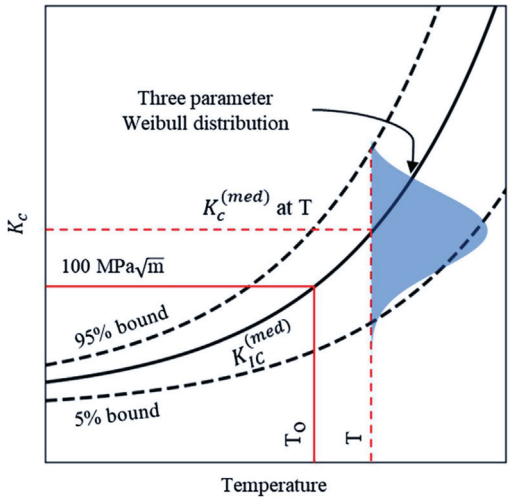

Fig. 7. Master curve per ASTM-E1921-20 (ASTM 2020a).

$$P_f = 1 - \exp\left\{-\int_0^B \left(\frac{K_I(x) - K_{\min}}{K_0 - K_{\min}}\right)^4 dx\right\} \tag{7}$$

where $K_I(x) = K_I$ field along the width of the flange. Fig. 8(a) shows the K_I field at the crack front of the representative splice detail (in Fig. 4) at three levels of applied major axis bending (without shear or axial force), corresponding to major axis moments of 33%, 47%, and 61% of the yield moment of the top section. The maximum flange stress $\sigma_{\text{flange}}^{\max}$ induced by each of these moments is shown in Fig. 8(a). Eq. (7) may be applied to the K_I fields at each of these moments to calculate the corresponding fracture probability. The above three loadings give fracture probabilities of 5%, 50%, and 95%. While Fig. 8(a) shows a single component of applied loading (i.e., major axis moment M_z), similar K_I field and fracture probabilities may be computed for an arbitrary set of loadings as defined by the vector of (P, M_z, M_x). The method may be conveniently extended to compute the fracture fragility curve for a given loading pattern by calculating fracture probabilities for a continuously increasing load factor applied to that loading pattern. For example, Fig. 8(b) shows the fracture fragility curve for a major axis moment applied to the representative splice detail (in the absence of any other load). Referring to this figure, the fragility curve is of an expected shape, with a median value at 47% of the major axis yield moment $M_{z,y}$ of the top section, indicating a 50% probability of fracture at an applied major axis moment of 2,470 kNm (1,822 kip-ft). The secondary horizontal axis in Fig. 8(b) is the maximum stress in the tension flange corresponding to the applied moments (on the primary axis). Thus, the fragility curve may be interpreted as a stress-fragility curve as well (in which $\sigma_{\text{flange,fracture}}^{\max}$ refers to the maximum stress over the flange at which the splice will fracture), albeit recognizing that this interpretation is particularized to a specific load pattern. Referring to these stress values, the median $\sigma_{\text{flange,fracture}}^{\max}$ is 180 MPa (26.1 ksi). As a point of interest, the configuration and material properties corresponding to Figs. 8(a and b) are nominally identical to those in Bruneau and Mahin's (1990) experiment on PJP splices. The moment at which the experiment fractured is indicated in Fig. 8(b); this corresponds to a roughly 99% probability of fracture as estimated by the framework. While a single data point is somewhat challenging to interpret against a fragility curve, the observation suggests that the fracture probabilities predicted by the tool are conservative. Possible sources of conservatism are summarized in the concluding

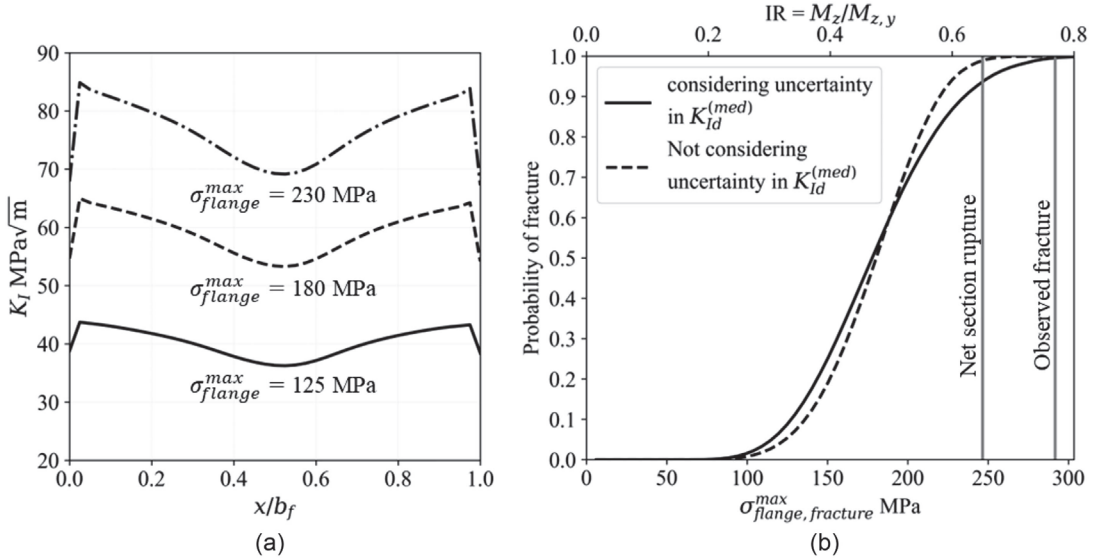

Fig. 8. (a) K_I fields generated from different pure bending loads; and (b) estimated fracture fragility for pure bending, CVN = 13.6 J at 21.1°C and LAST = 10°C.

section. Moreover, the Bruneau and Mahin (1990) study did not report the CVN impact energy of the material, further complicating interpretation of this result.

Incorporation of Uncertainty in Material Toughness Parameters

The probability of fracture described in the previous section assumes a given, deterministic estimate of $K_c^{(med)}$ at LAST for the weld material and considers effects of spatial variability over the flange width, conditional on this median value. However, estimation of $K_c^{(med)}$ in itself is subject to uncertainty (in addition to the spatial variability for a given $K_c^{(med)}$). For context, the SAC steel project (Fisher et al. 1995; Kaufmann et al. 1996, 1997) included material testing of the base and weld materials from the pre-Northridge moment frames. These provide important estimates of material toughness but suffer from the following limitations:

1. The toughness capacity is determined via the CVN impact energy. The CVN impact energy values (CVN hereafter) may be used as a measure of toughness capacity but cannot be directly used in a quantitative fracture mechanics framework.
2. The samples used for these studies are not extracted from PJP splice connections but from all-weld groove weld assemblies extracted from beam-column connection welds, in which the welding processes, deposition rates, weld passes, and heat input may be different from those for constructed splice connections.

These issues result in additional uncertainties and affect the probability of fracture of a given configuration and loading. To address the first issue, empirical correlations are used to establish the relationship between CVN and fracture toughness K_c. The lower-shelf or lower-transition toughness of ferritic steels is highly sensitive to the loading rate. Thus, a direct relationship between CVN (which is tested at dynamic rates) and $K_c^{(med)}$ (which reflects static toughness) is not readily available. A two-step correlation (Barsom and Rolfe 1999) must be used. This well-established procedure is shown in Fig. 9. Referring to the figure, the process involves two steps: (1) converting CVN to K_{Id} at the CVN test temperature, T_{CVN}, and (2) shifting K_{Id} to obtain K_c at $T_{\text{CVN}} - \text{T}_{\text{shift}}$. The value at the shifted temperature can then be used to estimate the reference temperature T_o of the master curve and hence $K_c^{(med)}$ (and the associated Weibull distribution) at any temperature [$K_c^{(med)}$ at LAST in Fig. 9(b)]. Features of this process, referred to as B&R correlation hereafter, are as follows:

- CVN to $K_{Id}^{(med)}$: Barsom (1975) determined the CVN $- K_{Id}$ lower bound correlation using test data for various grades of steel ranging in yield strength from 250 MPa (36 ksi) to 965 MPa (140 ksi), and eight heats of SA 533B, Class 1 steel with yield strength ranging from 440 MPa (64 ksi) to 500 MPa (72 ksi). The correlation (adjusted for SI units) is given by

$$K_{Id} = \sqrt{0.646 \times E \times \text{CVN}} \tag{8}$$

  where E is in MPa, CVN is in joules, and K_{Id} is in MPa$\sqrt{m}$ (The value 0.646 is converted from 5 in the original work for SI unit consistency). This lower bound correlation was intended to specify conservative, minimum toughness requirements. A best fit to the same data that is more suitable for probabilistic analysis, in contrast to the more conservative lower bound correlation suited for design and material specification, is given by Stillmaker et al. (2016) as

$$K_{Id} = \sqrt{0.979 \times E \times \text{CVN}} \tag{9}$$

  This correlation has a coefficient of variation (CV) of 0.11 around the mean estimate (Stillmaker et al. 2016). The mean estimate with the CV essentially represents the normal distribution of $K_{Id}^{(med)}$ at T_{CVN} given the CVN test values.
- $K_{Id}^{(med)}$ at T_{CVN} to $K_c^{(med)}$ at $T_{\text{CVN}} - T_{\text{shift}}$: (°C) is between the static and dynamic fracture toughness variation with temperature, in the lower-transition zone for steels with yield stress less than 965 MPa (140 ksi). It is a function of yield stress σ_{ys}, given by (Barsom and Rolfe 1970) as

$$T_{\text{shift}} = 101.7 - 0.121\sigma_{ys} \tag{10}$$

Eq. (10) has been converted from the original equation in imperial units ($T_{\text{shift}} = 215 - 1.5\sigma_{ys}$) for SI unit consistency. The temperature shift was determined using dynamic fracture toughness (K_{Id}) and linear elastic static fracture toughness (K_{Ic}) for ferritic steels. This may be conservative when estimating elastic-plastic

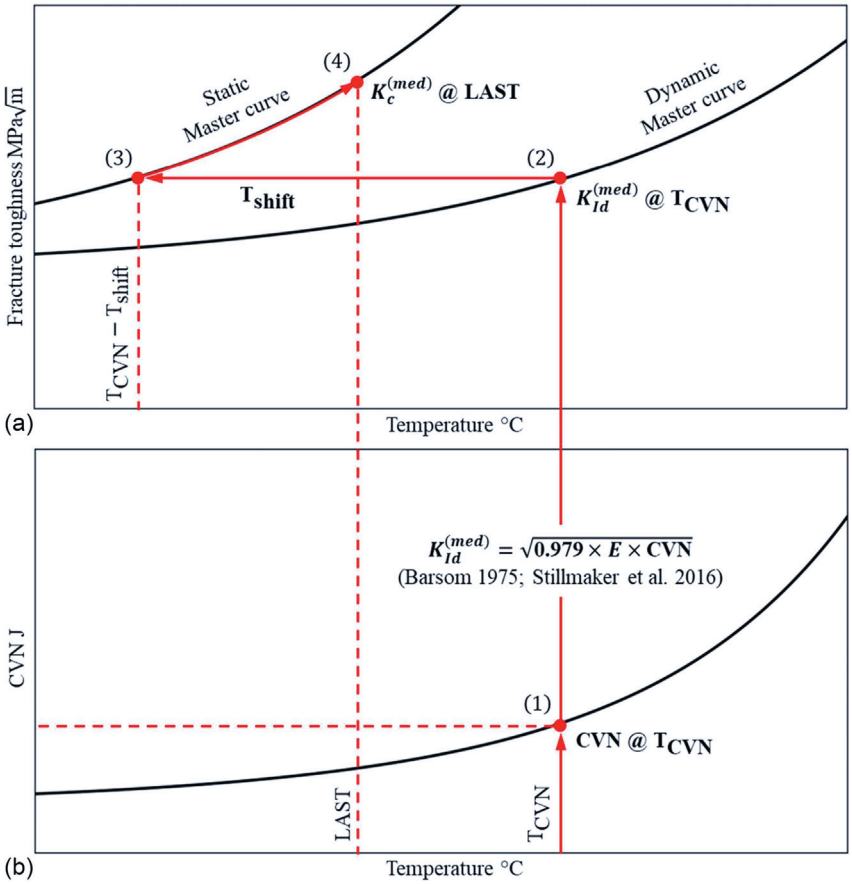

Fig. 9. Conversion of CVN at T_{CVN} to $K_c^{(med)}$ at LAST: (a) CVN at T_{CVN}; and (b) $K_{Id}^{(med)}$ at T_{CVN} from CVN $K_c^{(med)}$ at shifted temperature followed by $K_c^{(med)}$ at LAST from master curve.

equivalent static fracture toughness capacity (K_{Jc}), which is based on J integral. The static fracture toughness capacity is therefore denoted by the more generic K_c here. Eq. (11) is more generalized version of Eq. (10) which allows for the temperature shift to be calculated between static loading and an intermediate strain rate $\dot{\varepsilon}$ in the range $10^{-3}\ s^{-1} \le \dot{\varepsilon} \le 10\ s^{-1}$ (Barsom and Rolfe 1999) as

$$T_{\text{shift}} = (65.6 - 0.081\sigma_{ys})(\dot{\varepsilon})^{0.17} \tag{11}$$

Eq. (11) has been converted from imperial units, $T_{\text{shift}} = (150 - \sigma_{ys})(\dot{\varepsilon})^{0.17}$, for SI unit consistency. It should be noted that plane strain fracture toughness at a temperature is considered constant at strain rate equal to or lower than $10^{-5}\ s^{-1}$.

Once $K_c^{(med)}$ is determined at $T_{CVN}-T_{shift}$, Eq. (5) may be used to estimate the entire master curve, which allows estimation of $K_c^{(med)}$ at LAST. This is shown schematically in Fig. 9(b). It is important that the uncertainty in the $K_{Id}^{(med)}$ estimate is carried forward to the estimate of $K_c^{(med)}$ at LAST. This uncertainty is independent of the spatial randomness that is conditional on a deterministic value of $K_{Id}^{(med)}$. Considering toughness demands to be deterministic, Eq. (7) may be modified to determine the probability of fracture including the uncertainty in $K_{Id}^{(med)}$ as

$$P_f = \int_{-\infty}^{\infty} (P_f|_{K_{Id}^{(med)}}) f(K_{Id}^{(med)}) dK_{Id}^{(med)} \tag{12}$$

Computation of this probability is accomplished numerically through Monte Carlo simulation by varying $K_{Id}^{(med)}$ such that

$$P_f = \frac{1}{n}\sum_{i=1}^{n} P_f(K_c^{(med)(i)}) \tag{13}$$

where $K_c^{(med)(i)} = i$ sampled value of $K_c^{(med)}$; and n = number of sampled values. This Monte Carlo simulation is necessary because high-confidence static fracture toughness test data for the pre-Northridge weld filler material are not available. Conducting this simulation requires characterization of the probability distribution function $f(K_{Id}^{(med)})$ that reflects the uncertainty from various sources in $f(K_{Id}^{(med)})$. From the preceding discussion, the epistemic uncertainty—the error in correlation between CVN and $K_{Id}^{(med)}$ given by Eq. (9)—gives the distribution of $K_{Id}^{(med)}$ conditioned on a single value of CVN at T_{CVN}. It is noted here that CVN at T_{CVN} is currently assumed to be a single deterministic value based on the literature available for weldments in the pre-Northridge era (Fisher et al. 1995; Kaufmann et al. 1996, 1997). If improved data become available (e.g., through in situ testing of splice weldments), the value and uncertainty in CVN at T_{CVN} may be further refined and input to the process. Fig. 8(b) illustrates the effect of including the uncertainty in $K_{Id}^{(med)}$ per the process just detailed. Referring to this figure, the main effect of including this uncertainty is to flatten the fragility curve—slightly increasing the probability of failure at lower levels of loading and decreasing it at higher levels of loading. It is further noted here that the uncertainty in geometric parameters (e.g., weld penetration in the flange or the dimensions of the flanges) is not considered, mainly because this makes the Monte Carlo simulation highly expensive since it entails multiple

realizations of geometry, which must then be reflected in different FE models. This is assumed to be acceptable based on observations by Stillmaker et al. (2016) that suggest that the effect of uncertainties in geometric parameters (in reasonable and realistic ranges) on fracture probabilities is fairly modest relative to that of other parameters.

Fragility Assessment Tool

As shown in Fig. 3, the framework for fracture assessment effectively involves three steps: (1) generating a FEFM simulation model in Abaqus representing a splice configuration and loading, (2) characterizing the cleavage fracture probability of this splice configuration considering spatial variability and volume sampling effects, and (3) Monte Carlo simulation to incorporate the uncertainty in material toughness. While comprehensive, the application of this framework requires intensive, trained human input, which is costly and impractical for routine use in professional practice. To address this, a Python tool is developed that automates the entire process for the end user. Fig. 10 is a screenshot of the tool's input interface. Referring to this figure, the tool accepts user input pertaining to splice geometry, column height and splice location, material properties and loading (in terms of axial load P and column end moments M_{z1}, M_{z2} and M_{x1}, M_{x2} as shown in Fig. 10), and LAST (or the temperature of interest). Once provided with this input data, the script automatically generates the 3D FEFM model of the splice in Abaqus. Generation of a model algorithmically follows the best practices and quality controls (e.g., for mesh generation, material property assignments, boundary conditions) outlined previously. The tool submits the model for analysis after optional checks and confirmation from the user. The loading is applied in Abaqus in a proportional manner with respect to the input load vector (i.e., P, V_z, M_z, V_x, M_x generated from the input column axial load and end moments), using a load-factor that discretizes the load into 10 steps; a smaller step size is used if convergence is not achieved during any step of analysis. At each value of the load factor, the tool postprocesses the results to compute the K_I field over the width of the flange along the tip of the PJP flaw. This K_I field, along with CVN, is used to calculate the probability of splice fracture with the uncertainty in the CVN $- K_{Id}$ correlation incorporated using the Monte Carlo process described

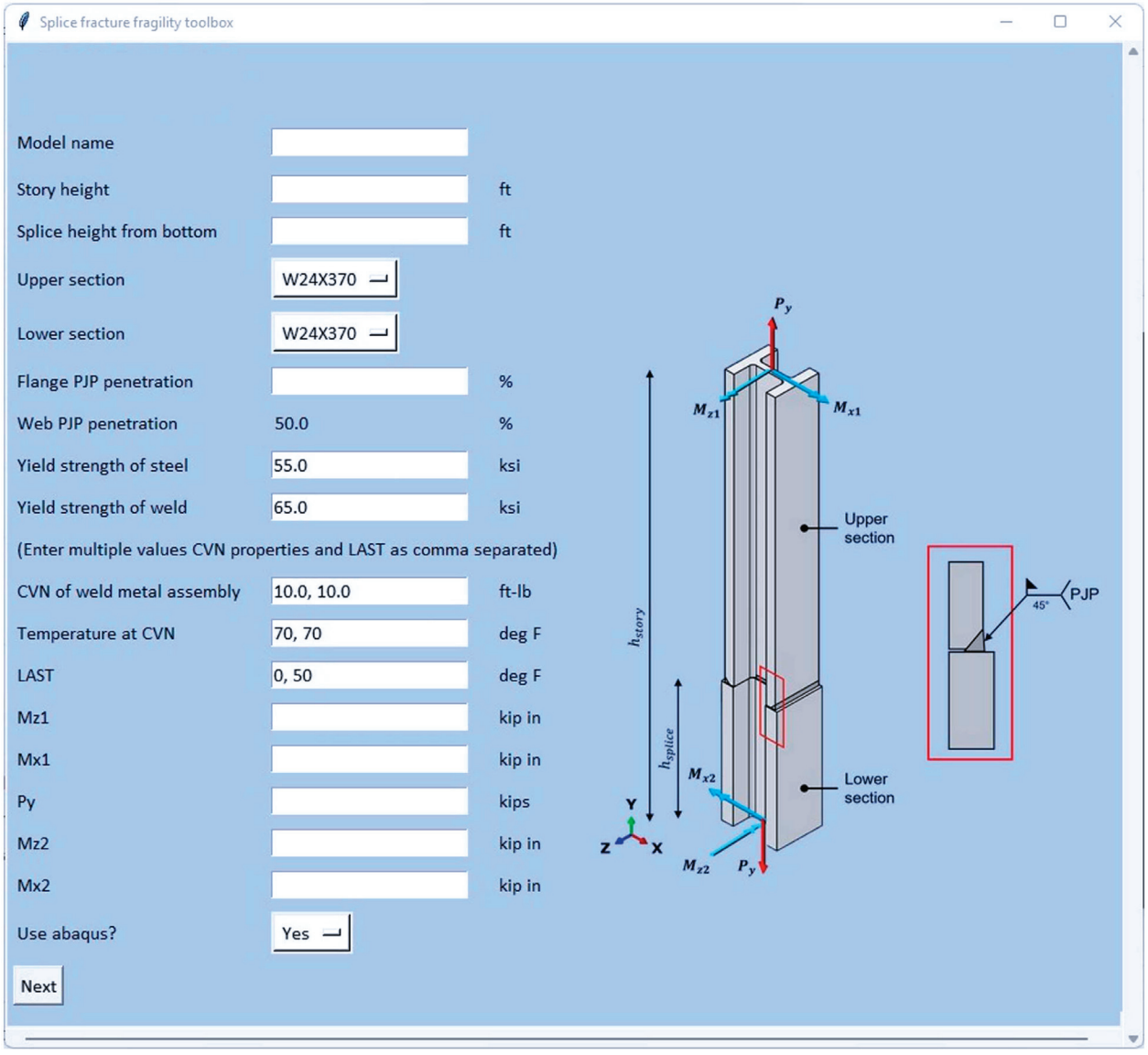

Fig. 10. Tool user interface.

J. Struct. Eng., 2023, 149(6): 04023062

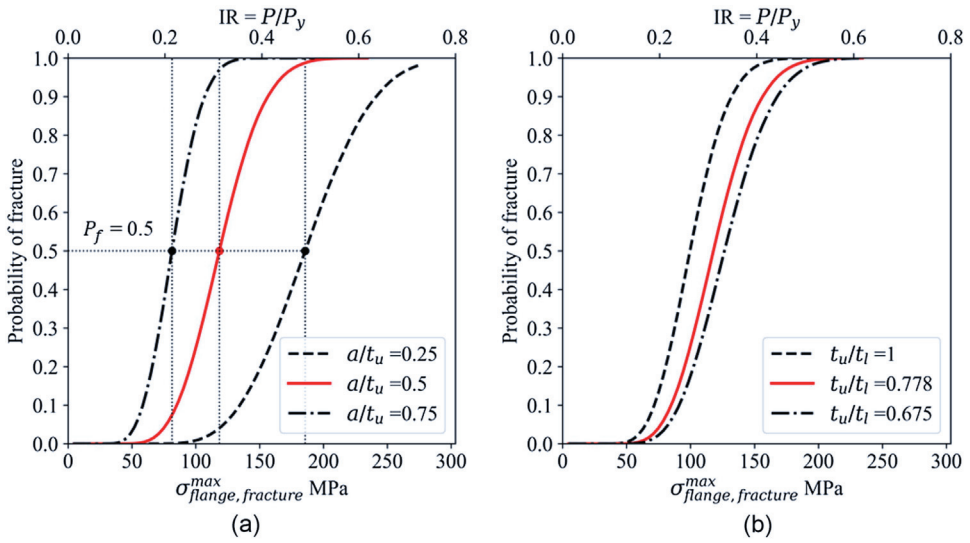

Fig. 11. Effect of geometric parameters on fracture fragility: (a) width ratio a/t_u; and (b) flange thickness ratio t_u/t_l. All plots generated for uniform tension loading and CVN = 13.6 J at 21.1°C and LAST = 10°C. Yield values calculated from expected yield strength, $f_{ys} = 380$ MPa .

in the previous section. This results in the calculation of net probability of fracture P_f at each load step, as well as a fracture fragility curve, with respect to the load factor. Figs. 11(a and b) show such fragility curves, whose quantitative aspects are discussed later. For now, the curves are discussed to illustrate the results that may be obtained from the fragility assessment tools. The curves in Fig. 11 are generated for splices subjected to uniform tension; the top horizontal axis shows the load factor in terms of a normalized axial load ratio, or interaction ratio (IR). The bottom horizontal axis shows the (maximum) stress in the flange, $\sigma^{\max}_{\text{flange,fracture}}$, as a secondary axis (which can be linearly mapped onto the axial load ratio), such that the curve may be interpreted as a stress-fragility curve, which may be more intuitive for some users. However, it is important that the stress-fragility curve interpreted in this manner is specific to a particular load pattern applied to the column—for example, if pure bending were applied to the column (as opposed to pure tension), a different stress-fragility curve would be obtained. The fragility assessment tool has some limitations. One, in order to reduce computational cost, only the flange located in the $+x$ direction [Fig. 5(a)] is modeled with refined mesh in the crack tip region (as discussed previously) to evaluate J-integral; the directions of the input load vector can be reversed by the user if the flange on the left-hand side is to be evaluated. Two, the probability of fracture, obtained as the output, is the probability of fracture of this flange only. The following section discusses key results obtained from the fragility assessment tool.

Results from Application of Fragility Assessment Tool

The main objectives of this section are to evaluate key factors that influence splice fragility, in terms of geometric, loading, and material parameters and, perhaps more important, to provide a sense of the capabilities of the tool to potential users as well as the types of information that may be obtained from it.

Geometric Factors

Figs. 11(a and b) show fracture fragility curves for the splice configuration shown in Fig. 4 loaded in pure tension. Fig. 11(a) shows the effect of crack width a on fracture fragility. Consequently, the three fragility curves in the figure have identical geometrical parameters (i.e., upper section, lower section, and web PJP) except for the crack width or the crack width ratio, a/t_u, where t_u is the thickness of the upper section flange. In Fig. 11(a), the effect of crack length on fracture is immediately apparent such that the configuration with the largest crack width has a fragility curve to the left of the other two. This is consistent with intuition and expected fracture response. Various statistics may be extracted from such curves; for example, Fig. 11(a) shows the median value of flange fracture stress for each of the three configurations, indicating that the lowest crack length (corresponding to $a/t_u = 0.25$) has a median stress value nearly 2.3 times that of the maximum crack length (corresponding to $a/t_u = 0.75$). Fig. 11(b) is similar to Fig. 11(a) except that it examines the effect of the flange thickness ratio t_u/t_l, where t_u and t_l are the respective thicknesses of the upper and lower section flanges. The fragility curves indicate that the equal flange condition ($t_u/t_l = 1$) is the more critical condition and that the fragility curves move right (i.e., indicate lower probabilities of fracture for a given flange stress) as the t_u/t_l ratio is reduced. This too is consistent with previous observations (e.g., Stillmaker et al. 2016) indicating that a thicker lower flange for the same crack width produces a reinforcing effect that reduces fracture toughness demand. While Figs. 11(a and b) are provided for a single base geometry, similar trends are observed across a wide range of column splice details.

Loading Parameters

Figs. 12(a and b) examine the effect of loading. Specifically, Fig. 12(a) compares fragility curves obtained for the splice configuration shown in Fig. 4 for uniform tension, pure uniaxial (major axis) bending, and a combination of axial tension and biaxial bending (applied in relative proportions such that $M_z/M_{z,y}$, $M_x/M_{x,y}$, and P/P_y at any instant in loading contribute equally to the IR, which is the sum of the three terms). In each case, fragility is interpreted with respect to the maximum stress, $\sigma^{\max}_{\text{flange,fracture}}$. From the fragilities, it is apparent that the difference in them between uniaxial bending and combined axial and bending is modest, whereas the uniform tension condition is significantly more critical. This may be attributed to the stress gradient in the flange (both in

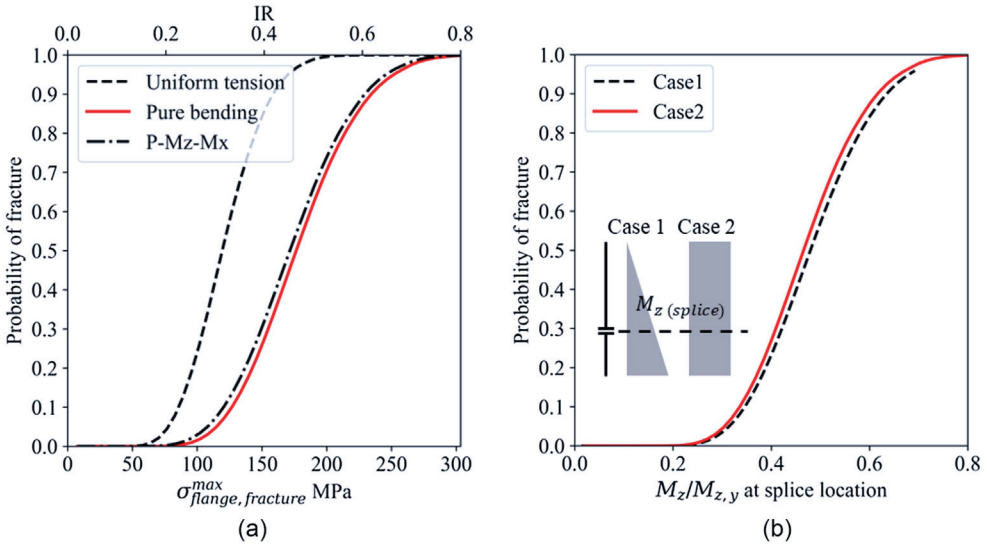

Fig. 12. Effect of loading type on fracture fragility: (a) uniform tension versus uniaxial and biaxial bending; and (b) joint shear. All plots generated for CVN = 13.6 J at 21.1°C and LAST = 10°C. Yield values calculated from expected yield strength f_{ys} = 380 MPa.

plane and out of plane) that occurs in the bending cases. This stress gradient has beneficial effects from the mechanistic standpoint—the gradient decreases the K_I at any location (e.g., Tada et al. 2000)—as well as the volume-sampling standpoint, because a smaller volume is subjected to high stress or K_I. This type of information may be used to evaluate, for example, results of 2D building simulations versus 3-D ones, which incorporate biaxial bending of the columns. Fig. 12(b) shows the effect of shear, where one configuration [identical to that in Fig. 11(a)] is subjected to uniform bending (i.e., no shear) and a moment gradient that induces a shear proportional to the applied moment such that $M/V = L$. Referring to the figure, the shear has only a negligible effect on the fracture fragilities. This observation is consistent across a range of configurations, suggesting that shear effects (at least within realistic ranges) may be disregarded in estimation of fracture fragilities.

Sensitivity to Material Fracture Parameters

The effect of material parameters is examined in four contexts pertaining to practical application: (1) CVN of the material, which serves as an indicator of the sensitivity to a basic measure of material toughness; (2) CV of $K_{Id}^{(med)}$ estimated from CVN, which shows sensitivity to uncertainty in the estimation of fracture toughness $K_c^{(med)}$; (3) service temperature, (LAST); and (4) assumed loading rate—the foregoing discussion assumes the seismic loading rate to be static, or a strain rate of zero for calculating $K_c^{(med)}$ at T-T_{shift} from $K_{Id}^{(med)}$ at T. Each of these effects is evaluated using the B&R correlation discussed previously. A subsequent subsection examines the impact of using alternate correlations between CVN and $K_c^{(med)}$.

The four effects just summarized are illustrated in Figs. 13(a–d). To facilitate convenient interpretation, a single base case (identified in Fig. 4) is considered, and subjected to two loading scenarios: uniform tension and pure uniaxial (major axis) bending. For each scenario, the median (corresponding to $P_f = 0.5$) maximum flange fracture stress, $\sigma^{max}_{flange,fracture}$, determined from the fragility assessment tool is plotted against the material variable of interest. Fig. 13(a) plots the median $\sigma^{max}_{flange,fracture}$ against the CVN value of the material measured at 21.1°C (70°F) and a LAST of 10°C (50°F). For reference, CVN values of pre-Northridge filler materials are in the range of 6.8–13.6 J (5–10 ft-lb) at 21.1°C (70°F). Referring to Fig. 13(a), a fairly strong positive trend is noted between CVN and the median fracture stress. In fact, for the pure bending case a CVN of ~24 J (17.5 ft-lb) is sufficient to mobilize net section fracture in the splice—that is, the fused ligament reaches its ultimate strength. On the other hand, the uniform tension case (referring to previous discussion) is more severe from the standpoint of splice fracture. Fig. 13(b) plots median fracture stress versus CV of $K_{Id}^{(med)}$ as the independent variable, holding mean $K_{Id}^{(med)}$ as 51.6 MPa$\sqrt{\text{m}}$ (47 ksi $\sqrt{\text{in.}}$), obtained from Eq. (9), using a CVN of 13.6 J (10 ft-lb) at 21.1°C (70°F). This is pertinent because conducting K_{Jc}/K_{Ic} or K_{Id} tests is expensive (compared to CVN tests). On the other hand, converting CVN to $K_{Id}^{(med)}$ through correlation, as discussed previously, introduces additional uncertainty in the estimate of $K_{Id}^{(med)}$. As a result, it is of practical value to understand the importance of accurate characterization of $K_{Id}^{(med)}$ when estimating fracture fragility. In this context, Fig. 13(b) indicates a relatively weak dependence of median fracture stress (for both uniform tension and pure bending) on CV in $K_{Id}^{(med)}$ given a median value. As expected, higher CV (or variability) results in lower median fracture stress. This is a well-known effect of weakest-link sampling (Beremin et al. 1983) where higher variability increases the probability of a weaker link being sampled. Nonetheless, the trends observed are weak, suggesting that expensive K_{Jc}/K_{Ic} or K_{Id} testing may not be warranted for assessing splice fracture fragility. Fig. 13(c) plots median fracture capacity against LAST—that is, the operating temperature of the building at the time of the expected earthquake. As expected, there is a positive and steady increase in median fracture capacity with respect to LAST.

Fig. 13(d) shows the effect of assumed loading rate in the splice. It is similar to Figs. 13(a–c) in that it plots median flange fracture stress $\sigma^{max}_{flange,fracture}$ (for both types of loading: uniform tension and pure bending) against the strain rate (at which K_c is determined) assumed in the B&R correlation. The strain rate ranges from a minimum $10^{-6}\ s^{-1}$ (i.e., the static assumption used in previous analysis) to 10 s^{-1}. For reference, a strain rate of $10^{-3}\ s^{-1}$ [the vertical line in Fig. 13(d)] is consistent with expectations in seismic events, assuming a period of vibration of 1 s, which is typical of mid- to

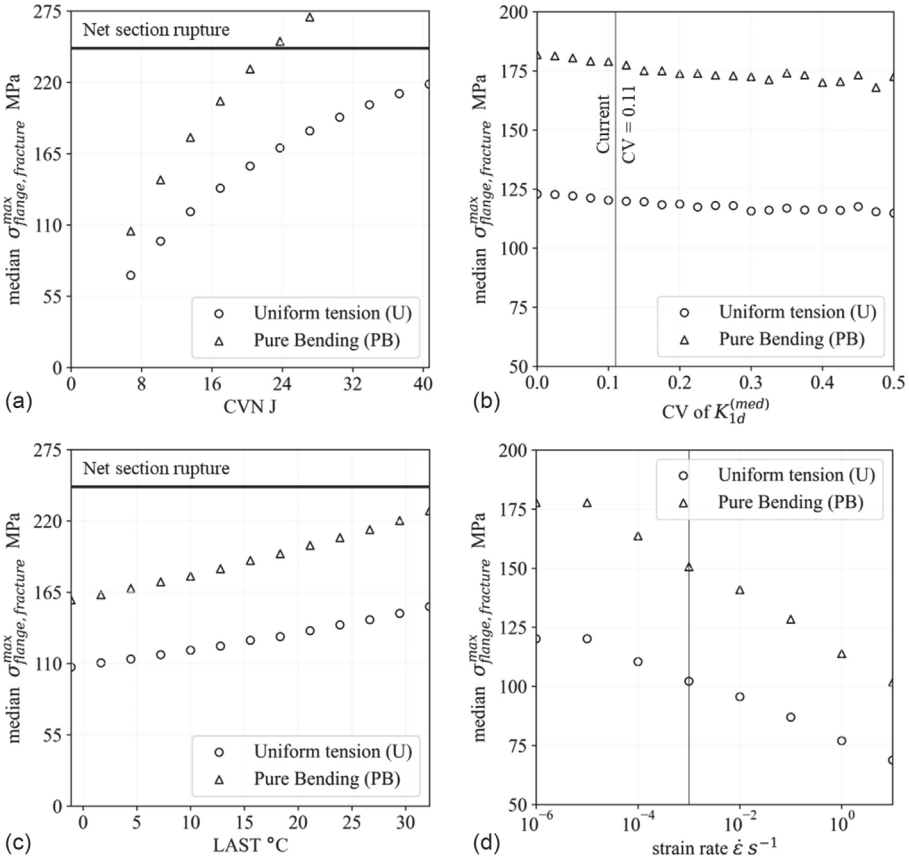

Fig. 13. Effect of material parameters on median $\sigma^{\max}_{\text{flange,fracture}}$: (a) CVN at 21.1°C and LAST = 10°C; (b) CV of $K_{1d}^{(med)}$ for CVN = 13.6 J at 21.1°C and LAST = 10°C; (c) LAST for CVN = 13.6 J at 21.1°C; and (d) strain rate at CVN = 13.6 J at 21.1°C and LAST = 10°C.

high-rise buildings, along with a stress amplitude of 0.5 times the yield stress. Referring to Fig. 13(d), it is evident that strain rate has a notable effect on median fracture stress. Specifically, $10^{-3}\ s^{-1}$ reduces the median fracture stress obtained from the static loading assumption by 15%.

Effect of Alternate Correlations in Converting CVN to $K_c^{(med)}$

The results presented so far are all based on a modified two-step B&R correlation to convert CVN to $K_c^{(med)}$. While the B&R correlation remains popular in the United States, over the last 50 years other CVN to K_c correlations have been developed (see Collins et al. 2016 for a summary). One is presented in Annex J of BS 7910 (BSI 2019), which is used in the United Kingdom. Before results from the BS 7910 correlation are compared with the B&R correlation, some context is useful. Specifically, similar to the original B&R correlation [Eq. (8)], the correlation method presented in Annex J.2.1 of BS 7910 is a direct correlation that predicts the *lower bound* of static fracture toughness $K_c^{(med)}$ given CVN at a service temperature; this is done by fitting curves that bracket all the data used in establishing the correlation in a lower-bound sense. As discussed previously, such correlations are suitable for establishing acceptability criteria or material toughness specifications. On the other hand, *best-fit* correlations are more appropriate for use in a probabilistic framework that aims to characterize the full distribution of failure. Stillmaker et al.'s (2016) modification to the B&R correlation [Eq. (9)] is an example. This is an important distinction because it indicates that comparing results from a lower-bound correlation (e.g., BS 7910) to those from a best-fit correlation is not appropriate. To address this issue effectively, two variants of the BS 7910 correlation are considered in this study.

The first is the original BS 7910 correlation, which directly converts CVN to $K_c^{(med)}$ at service temperature T_{CVN} using the following equation:

$$K_c = 12\sqrt{\text{CVN}} \tag{14}$$

Once $K_c^{(med)}$ is determined at T_{CVN}, Eq. (5) may be used to estimate the reference temperature, T_o, which allows estimation of $K_c^{(med)}$ at LAST.

The second is a best-fit modification to the BS 7910 approach, which is analogous to the Stillmaker et al. (2016) modification to the B&R correlation. This involves reducing the reference temperature obtained from Eqs. (14) and (5) by a temperature adjustment T_{adj} before estimating $K_c^{(med)}$ at LAST. The T_{adj} is determined using predicted and actual T_o for the historical bridge steel fracture database of Collins et al. (2016). In addition, the standard deviation of scatter around the adjusted T_o is provided, which may be used to perform Monte Carlo simulations on the adjusted T_o.

Once the two variants of the BS 7910 correlation have been developed to generate estimates of $K_c^{(med)}$, they may be used in a manner similar to the best-fit B&R approach to generate estimates of $\sigma^{\max}_{\text{flange,fracture}}$ corresponding to a given fracture probability. A random set of 25 splice configurations, each loaded in uniform tension and pure uniaxial bending (major axis), is generated that samples a/t_u, t_u/t_l, and t_u over a wide range such that the 25 configurations provide a general sense of the underlying trends. For each of these,

J. Struct. Eng., 2023, 149(6): 04023062

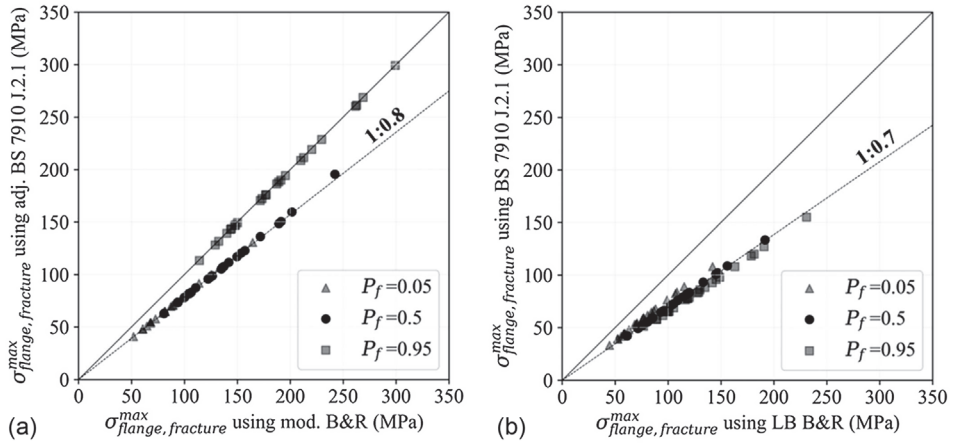

Fig. 14. Comparison of fracture stress at different fracture probabilities for splice configurations subjected to uniform tension: (a) best-fit (modified) B&R and best-fit (adjusted) BS 7910; and (b) original (lower-bound) B&R and original BS 7910 (CVN = 13.6 J at 21.1°C and LAST = 10°C).

5%, 50% (median), and 95% percentile $\sigma^{max}_{flange,fracture}$ values are determined from the two BS 7910 variants and from the best-fit and original lower-bound B&R approaches. Figs. 14(a and b) plot these against each other for one material parameter case—CVN of 13.6 J (10 ft-lb) at 21.1°C (70°F) and LAST of 10°C (50°F)—and one loading scenario—uniform tension. Fig. 14(a) compares the results from the best-fit B&R correlation with those from the best-fit BS 7910 correlation as summarized previously. Both cases include Monte Carlo simulation of the uncertain parameter estimate. Fig. 14(b) compares results from the original (lower-bound) B&R correlation with those from the original BS correlation [Eq. (14)]. Presenting the results in this manner ensures a meaningful comparison. Referring to Figs. 14(a and b), the following may be noted:

- Best-fit BS 7910 estimates nearly the same fracture stress as best-fit B&R at a high probability of fracture ($P_f = 0.95$). However, at a lower probability ($P_f = 0.05$ and 0.5), the fracture stress values estimated from BS 7910 are 80% of the values obtained from B&R, indicating a degree of conservatism.
- The original BS 7910 correlation estimates fracture stresses that are 70% of the stresses estimated by the original lower bound B&R correlation across all probabilities of fracture.

In summary, the choice of correlation has a significant effect on of fracture probability estimation. This may be attributed to many factors, including the functional forms as well as the original data sets they were calibrated to. Without additional test data (specifically in situ material fracture properties in splices), it is difficult to ascertain the appropriate approach.

Sensitivity to Other Parameters

In addition to key parameters, sensitivity studies have revealed less important parameters. Consequently, dependencies on these parameters have not been explicitly discussed . However, it is important to note them in the interest of completeness and also for informing intuition regarding the fracture of these connections. Specifically,

- Presence versus absence of reinforcing bevel—resulting in a maximum variation of <1% in fracture fragilities (i.e., <1% change in stress for each probability level).
- Yield strength of steel—5% and 95% values (Jaquess and Frank 1999): 331 MPa (42 ksi) and 427 MPa (62 ksi), respectively, resulting in a maximum variation of <1% in in fracture fragilities compared with the fracture fragility obtained using expected yield strength, 380 MPa (55 ksi); it should be noted that the fracture fragilities were generated using a CVN of 13.6 J (10 ft-lb) at 21.1°C (70°F) and a LAST of 10°C (50°F). The difference increases at higher probabilities of fracture and at higher toughness capacities.
- Standard deviation in estimate of T_{shift}—incorporating variation in the empirical relationship relating T_{shift} to yield strength [Eq. (10)] resulted in a maximum variation of <1.5% in median flange fracture stress. The standard deviation was varied up to 14°C (25°F), with the standard deviation from the data used to develop the correlation (Barsom and Rolfe 1999), being 9.5°C (17.1°F).

Comparison of ATC 114 and Fragility Assessment Tool

As discussed in the Introduction, ATC 114 (ATC 2017), which is the only official guidance regarding pre-Northridge splices, provides simplified equations to assess fracture in those splices. These equations do not consider several effects that are incorporated into the new fracture assessment framework and tool, so it is useful to compare key outputs from ATC 114 against their counterparts from the fragility assessment tool. It is important that ATC 114 itself does not develop fragility curves; rather, three values of K_{Ic} (corresponding to 5%, 50%, and 95% probabilities of exceedance) are recommended, which may then be used to determine fracture stresses that implicitly correspond to these probabilities of exceedance. The K_{Ic} values provided in ATC 114 are conditional on a CVN of 13.6 J (10 ft-lb) at 21.1°C (70°F), which is equal to the default value used in the proposed framework; they are assumed to follow a Weibull distribution based on the master curve. As a result, fracture fragility curves may be developed based on ATC 114 by conducting equal probability mapping of the underlying Weibull distribution of K_{IC} (as implied by the ATC 114 values) through the simplified equations for fracture stress. Fig. 15(a) shows such a fragility curve generated for the example splice configuration in Fig. 4. Also shown are fragility curves for the same splice configuration, loaded in uniform tension and pure bending. The fragility curves for the same splice configuration under uniform tension and pure bending are also shown. These curves explicitly incorporate through width effects, in-plane stress gradients, and volume sampling. In Fig. 15(a), the ATC 114 fragility curve (which does not distinguish between uniform tension and pure bending) is well to the left of the two fragility curves generated by the proposed framework for uniform tension and pure bending, suggesting that

J. Struct. Eng., 2023, 149(6): 04023062

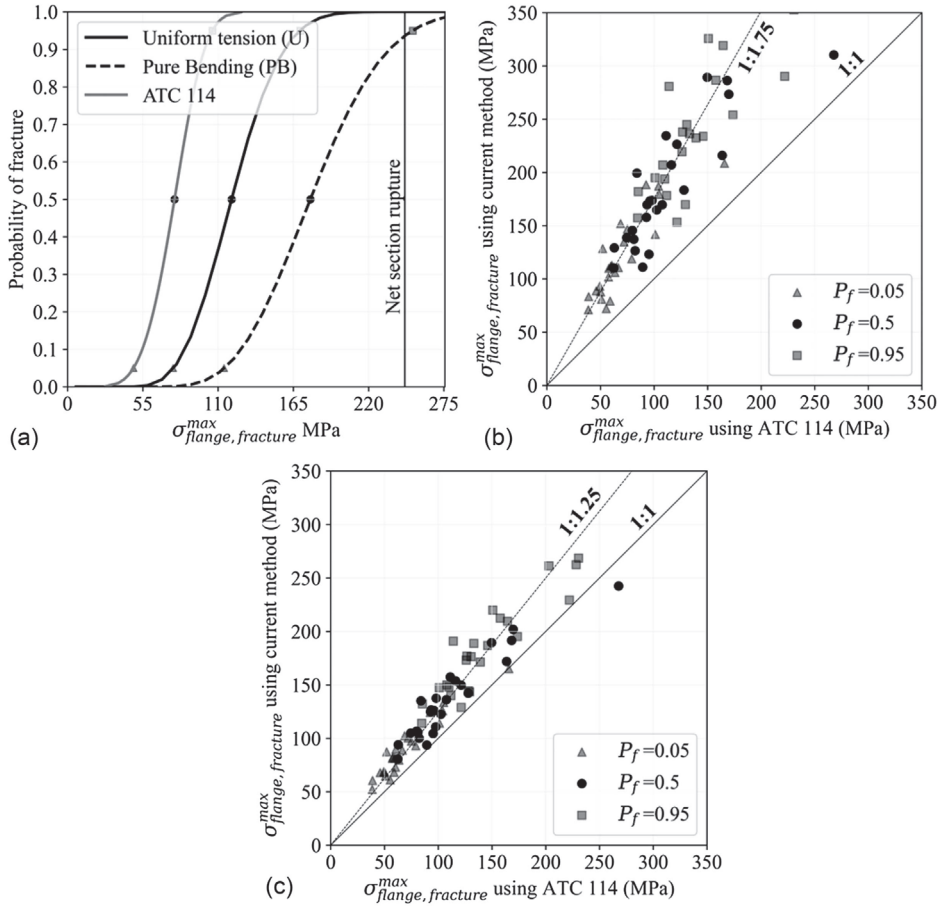

Fig. 15. (a) Comparison of fracture fragility obtained using current framework and ATC 114 for example splice; (b) comparison of fracture stress at different fracture probabilities for splice configurations subjected to pure bending loading; and (c) comparison of fracture stress at different fracture probabilities for splice configurations subjected to uniform tension loading (CVN = 13.6 J at 21.1°C and LAST = 10°C).

ATC 114 is conservative in this case. Percentile $\sigma^{\max}_{\text{flange,fracture}}$ may be recovered from each curve and then compared across a range of splice configurations to examine trends between ATC 114 and the proposed framework. The 5%, 50% (median), and 95% percentile $\sigma^{\max}_{\text{flange,fracture}}$ values are determined from the ATC 114 equations and from the fragility assessment tool for the set of 25 splice configurations defined previously. Figs. 15(b and c) plot these against each other for the uniform tension and pure bending cases, respectively. While these results are plotted for one case—a CVN of 13.6 J (10 ft-lb) at 21.1°C (70°F) and LAST of 10°C (50°F), similar trends are recovered for other material parameters as well. From the figures, it is evident that the current guideline (ATC 114) generally underestimates the fracture capacity of the splices at all probabilities. On average, ATC 114 underestimates median $\sigma^{\max}_{\text{flange,fracture}}$ by 19%, and 5% and 95% $\sigma^{\max}_{\text{flange,fracture}}$ by 23% and 20%, respectively, for the uniform tension case. These values change to 42%, 45%, and 43% (median, 5%, and 95%) for the pure uniaxial bending case, suggesting that for bending-induced fracture (which is likely more common), the ATC equations are significantly conservative. In Fig. 12(a), biaxial bending produces results very similar to uniaxial bending (in terms of fragility with respect to peak stress), suggesting a similar conservatism for biaxial bending. While this is reassuring from the standpoint of safety, it suggests that (compared with the tool) ATC 114 (when given the same inputs of material properties, geometry, and loading) may indicate a retrofit, even when it is not warranted.

Summary, Conclusions, and Limitations

The fracture potential of pre-Northridge PJP-welded column splices is of concern due to the presence of large flaws (with 25%–75% flange penetrations) and the low-toughness materials used in that era. Accurately assessing the fracture risk of these splices is particularly important because repair is highly disruptive to building operations. However, existing guidance (ATC 2017) on assessing the fracture risk of these connections is sparse and based on very limited experimental data and finite-element simulations that do not consider important aspects of response, including 3D effects (loading as well as out-of-plane stress gradients) and material volume sampling. Moreover, the existing guidance is based primarily on test and simulation data for prospective PJP weld connections with tougher welds and lower flaw sizes (80%–90% flange penetrations), and with beveled transitions between the flanges, which are typically absent in pre-Northridge connections. As a result, the accuracy of the (ATC 2017) guidance bears further study.

Motivated by this, a comprehensive framework to assess the fracture risk of pre-Northridge PJP splices is presented. The framework addresses the key issues not considered in previous research, specifically3D effects and volume sampling. This is accomplished by first conducting 3D FEFM simulations of splice details which characterize through-width fracture toughness demand (K_I) fields under a range of loadings. These fields are then processed through a weakest-link construct based on the master curve (Wallin 1998) to

estimate a probability of failure for the splice. Uncertainties in fracture toughness estimation (due to conversion from CVN energy to K_c) are incorporated by Monte Carlo simulation. The resulting framework is implemented in a Python-based tool that automatically generates FEFM models, runs them, and then conducts Monte Carlo simulations to generate fracture fragilities for an arbitrary splice detail and arbitrary loadings. The tool is designed for use in professional practice, where the high human input needed for development of FEFM models may be prohibitively costly. The tool (and the underlying framework) is then applied to a range of configurations and loadings to examine the effects of various geometric, material, and loading parameters. An important finding is that the proposed framework, when considered over a range of splice configurations, results in median flange fracture stresses (i.e., capacities) that are roughly 43% larger when the splices are subjected to pure bending loads and 19% larger when subjected to uniform tension than those in ATC (2017) guidance. This suggests that the new framework mitigates ATC 2017's significant conservatism and may influence repair or retrofit decisions. The tool and the framework are designed to be transparent in methodology and modular in intellectual development as well as implementation, such that they may be refined as new experimental data or information becomes available. It is anticipated that the tool (and its future refinements) will be used to support decisions not only in PJP splice risk mitigation but also in parametric studies that inform prospective experimental programs and investments toward obtaining material data (e.g., measurements of in-situ fracture toughness) to optimize estimates of fracture risk.

It is important to discuss the limitations of the framework. Some pertain to the FEFM simulations, specifically that (1) residual stresses are not considered, but it may be argued that the root pass of the weld (at the flaw) is likely in compression such that this simplification is conservative; (2) the simulations assume that the unfused flaw acts as a sharp crack, thereby justifying the use of conventional fracture mechanics, but this may be a conservative assumption; and (3) effects such as weld anisotropy are not considered in the constitutive model. These assumptions are made because of the lack of data needed to definitively assess the effect of these issues and the near absence (except the Bruneau and Mahin 1990 test) of any large-scale data for these types of connections. From a methodological point of view, one limitation is that uncertainty in geometric parameters (especially flaw size) is not considered. Stillmaker et al. (2016) showed that this does not significantly alter fracture probabilities. Another limitation pertains to characterization of the material parameters. There are numerous issues in this regard, including conversion of CVN energy to fracture toughness parameters, and how well these inferred fracture toughness parameters represent the true in-situ toughness of the deposited weld material or heat-affected zone. Regarding the former, an alternate CVN-K_c correlation is explored. A third limitation is the use of monotonic fracture mechanics to represent cyclic earthquake-induced failure. This may be justified because the computed fracture stress is well below the yield stress; however, some degree of reversed crack tip plasticity cannot be ruled out. Resolution of these issues is not possible without verification against experimental data; in fact, the single available experimental data point (while difficult to interpret) indicates that the proposed framework estimates fracture risk in a conservative way. It is hoped that as experimental data become available, the framework and tool will be refined. In the meantime, they address an urgent need of the professional community. In closing, it is noted that the fracture assessment tool (with its underlying framework) is only one part of a prospective decision support framework for risk mitigation that will use other tools (including building performance assessment and hazard analysis) to inform trade-offs between fracture risk and costs of intervention.

Data Availability Statement

Some or all data, models, or code that support the findings of this study are available from the corresponding author upon reasonable request.

Acknowledgments

The authors are grateful to the Pacific Earthquake Engineering Center (Grant No. 1158-NCTRVI) and the National Science Foundation (Grant No. 2129445) for their support. Input from James Malley and Robert Pekelnicky of Degenkolb Engineers, and Masume Dana and Ali Roufigarinejad of Forell Elsesser Engineers is greatly appreciated. The findings presented in this paper do not reflect those of the sponsors and are solely those of the authors.

References

AISC. 2016. *Seismic provisions for structural steel buildings*. AISC 341-16. Chicago: AISC.

Anderson, T. L. 2017. *Fracture mechanics: Fundamentals and applications*. Boca Raton, FL: CRC Press.

ASTM. 2020a. *Standard test method for determination of reference temperature for ferritic steels in the transition range*. ASTM E1921-20. West Conshohocken, PA: ASTM.

ASTM. 2020b. *Standard test method for measurement of fracture toughness*. ASTM E1820-20b. West Conshohocken, PA: ASTM.

ATC (Applied Technology Council). 2017. *Guidelines for nonlinear structural analysis for design of buildings: Part II a—Steel moment frames*. NIST GCR 17-917-46v2 (ATC 114). Gaithersburg, MD: National Institute of Standards and Technology.

ATC (Applied Technology Council). 2022. *Research plan for the study of pre-Northridge earthquake weak panel zones and welded column splices with PJP groove welds (Request for proposal)*. ATC 153. Gaithersburg, MD: National Institute of Standards and Technology.

Barsom, J., and S. Rolfe. 1970. *Correlations between KIc and Charpy V-notch test results in the transition-temperature range*, 281–302. West Conshohocken, PA: ASTM.

Barsom, J. M. 1975. "Development of the AASHTO fracture-toughness requirements for bridge steels." *Eng. Fract. Mech.* 7 (3): 605–618. https://doi.org/10.1016/0013-7944(75)90060-0.

Barsom, J. M., and S. T. Rolfe. 1999. *Fracture and fatigue control in structures: Applications of fracture mechanics*. West Conshohocken, PA: ASTM.

Beremin, F., A. Pineau, F. Mudry, J.-C. Devaux, Y. D'Escatha, and P. Ledermann. 1983. "A local criterion for cleavage fracture of a nuclear pressure vessel steel." *Metall. Trans. A* 14 (11): 2277–2287. https://doi.org/10.1007/BF02663302.

Brocks, W., and I. Scheider. 2003. "Reliable J-values—Numerical aspects of the path-dependence of the J-integral in incremental plasticity." *Mater. Test* 45 (6): 264–275. https://doi.org/10.1515/mt-2003-450608.

Bruneau, M., and S. A. Mahin. 1990. "Ultimate behavior of heavy steel section welded splices and design implications." *J. Struct. Eng.* 116 (8): 2214–2235. https://doi.org/10.1061/(ASCE)0733-9445(1990)116:8(2214).

BSI (British Standards Institution). 2019. *Guide on methods for assessing the acceptability of flaws in metallic structures*. BS 7910. London: BSI.

Chi, W.-M., and G. G. Deierlein. 2000. *Integration of analytical investigations on the fracture behavior of welded moment resisting connections*. Stanford, CA: Blume Earthquake Engineering Center.

Chi, W.-M., G. G. Deierlein, and A. Ingraffea. 2000. "Fracture toughness demands in welded beam-column moment connections." *J. Struct. Eng.* 126 (1): 88–97. https://doi.org/10.1061/(ASCE)0733-9445(2000)126:1(88).

Chisholm, M. P., R. G. Pekelnicky, and J. O. Malley. 2017. "High-rise pre-Northridge partial joint penetration column splice repair." In *Proc., SEAOC 2017*. Sacramento, CA: Structural Engineers Association of California.

Collins, W., R. Sherman, R. Leon, and R. Connor. 2016. "State-of-the-art fracture characterization. II: Correlations between Charpy V-notch and the master curve reference temperature." *J. Bridge Eng.* 21 (12): 04016098. https://doi.org/10.1061/(ASCE)BE.1943-5592.0000955.

Fisher, J., R. Dexter, and E. Kaufmann. 1995. *Fracture mechanics of welded structural steel connections*. Rep. No. 95-09. Sacramento, CA: SAC Joint Venture.

Galasso, C., K. Stillmaker, C. Eltit, and A. Kanvinde. 2015. "Probabilistic demand and fragility assessment of welded column splices in steel moment frames." *Earthquake Eng. Struct. Dyn.* 44 (11): 1823–1840. https://doi.org/10.1002/eqe.2557.

Hutchinson, J. W. 1968. "Singular behaviour at the end of a tensile crack in a hardening material." *J. Mech. Phys. Solids* 16 (1): 13–31. https://doi.org/10.1016/0022-5096(68)90014-8.

IAEA (International Atomic Energy Agency). 2005. *Guidelines for application of the master curve approach to reactor pressure vessel integrity in nuclear power plants*. Rep. No. Series No. 429. Vienna, Austria: IAEA.

Jaquess, T. K., and K. Frank. 1999. *Characterization of the material properties of rolled sections*. SAC/BD-99/07. Sacramento, CA: SAC Joint Venture.

Kanvinde, A. M., B. V. Fell, I. R. Gomez, and M. Roberts. 2008. "Predicting fracture in structural fillet welds using traditional and micromechanical fracture models." *Eng. Struct.* 30 (11): 3325–3335. https://doi.org/10.1016/j.engstruct.2008.05.014.

Kaufmann, E. J., J. W. Fisher, R. M. Di Julio, and J. L. Gross. 1997. *Failure analysis of welded steel moment frames damaged in the Northridge earthquake*. NISTIR 5944. Gaithersburg, MD: National Institute of Standards and Technology.

Kaufmann, E. J., M. Xue, L.-W. Lu, and J. W. Fisher. 1996. "Achieving ductile behavior of moment connections." *Mod. Steel Constr.* 36 (1): 30–39.

Kirk, M. 2002. *The technical basis for application of the master curve to the assessment of nuclear reactor pressure vessel integrity.* ADAMS ML093540004. Washington, DC: United States Nuclear Regulatory Commission.

Maison, B., K. Kasai, R. J. Dexter, A. Ingraffea, and G. G. Deierlein. 1996. *Selected results from the SAC phase 1 beam-column connection pre-test analyses*. SAC/BD-96/01. Sacramento, CA: SAC Joint Venture.

McMeeking, R., and D. Parks. 1979. "On criteria for J-dominance of crack-tip fields in large-scale yielding." *Elastic-Plast. Fract.* 668 (Jun): 175–194. https://doi.org/10.1520/STP35830S.

Nudel, A., M. Dana, and L. Maclise. 2013. "Adaptive reuse: Creating a New School of Dentistry in an Outdated Urban Office Building." In *Proc., SEAOC 2013*. Sacramento, CA: Structural Engineers Association of California.

Nuttayasakul, N. 2000. *Finite element fracture mechanics study of partial penetration welded splice*. Stanford, CA: Stanford Univ.

Rice, J. R., and G. F. Rosengren. 1968. "Plane strain deformation near a crack tip in a power-law hardening material." *J. Mech. Phys. Solids* 16 (1): 1–12. https://doi.org/10.1016/0022-5096(68)90013-6.

SAC Joint Venture. 1995a. *Analytical and field investigations of buildings affected by the Northridge earthquake of January 17, 1994*. Rep. No. 95–04. Sacramento, CA: SAC Joint Venture.

SAC Joint Venture. 1995b. *Technical report: Case studies of steel moment-frame building performance in the Northridge earthquake of January 17, 1994*. Rep. No. 95–07. Sacramento, CA: SAC Joint Venture.

SAC Joint Venture. 2000a. *Recommended seismic design criteria for new steel moment-frame buildings*. FEMA 350. Sacramento, CA: SAC Joint Venture.

SAC Joint Venture. 2000b. *Recommended seismic evaluation and upgrade criteria for existing welded steel moment-frame buildings*. FEMA 351. Sacramento, CA: SAC Joint Venture.

Shaw, S. M., K. Stillmaker, and A. M. Kanvinde. 2015. "Seismic response of partial-joint-penetration welded column splices in moment-resisting frames." *Eng. J.* 52 (2): 87–108.

Shen, J., T. A. Sabol, B. Akbas, N. Sutchiewcharn, and W. Cai. 2010. "Seismic demand on column splices in steel moment frames." *Eng. J.* 47 (4): 223.

Stillmaker, K., A. Kanvinde, and C. Galasso. 2016. "Fracture mechanics-based design of column splices with partial joint penetration welds." *J. Struct. Eng.* 142 (2): 04015115. https://doi.org/10.1061/(ASCE)ST.1943-541X.0001380.

Tada, H., P. C. Paris, and G. R. Irwin. 2000. *The stress analysis of cracks handbook*. New York: ASME Press.

Wallin, K. 1984. "The scatter in KIC-results." *Eng. Fract. Mech.* 19 (6): 1085–1093. https://doi.org/10.1016/0013-7944(84)90153-X.

Wallin, K. 1985. "The size effect in KIC results." *Eng. Fract. Mech.* 22 (1): 149–163. https://doi.org/10.1016/0013-7944(85)90167-5.

Wallin, K. 1993. "Irradiation damage effects on the fracture toughness transition curve shape for reactor pressure vessel steels." *Int. J. Press. Vessels Pip.* 55 (1): 61–79. https://doi.org/10.1016/0308-0161(93)90047-W.

Wallin, K. 1998. *Master curve analysis of ductile to brittle transition region fracture toughness round robin data. The "EURO" fracture toughness curve*. Otamiemi, Espoo, Finland: VTT Technical Research Centre of Finland.